# In-silico calculation of soil pH by SCEPTER v1.0

Yoshiki Kanzaki[1], Isabella Chiaravalloti[2,3], Shuang Zhang[4], Noah J. Planavsky[2,3], Christopher T. Reinhard[1]

[1]School of Earth and Atmospheric Sciences, Georgia Institute of Technology, Atlanta, GA 30332, USA
5   [2]Department of Earth and Planetary Sciences, Yale University, New Haven, CT 06511, USA
[3]Yale Center for Natural Carbon Capture (YCNCC), Yale University, New Haven, CT 06511, USA
[4]Department of Oceanography, Texas A&M University, College Station, TX 77843, USA

*Correspondence to*: Yoshiki Kanzaki (ykanzaki3@gatech.edu), Christopher T. Reinhard (chris.reinhard@eas.gatech.edu)

**Abstract.** One of the soil properties most commonly measured to describe agronomic and biogeochemical conditions of
10   soils is "soil pH". Soil pH measures the concentration of exchangeable $H^+$ that resides in bulk soil samples taken from the
field, through aqueous $H^+$ measurements of extractants (e.g., deionized water or electrolyte solutions) added to dried bulk
soil samples in the laboratory. Therefore, "soil pH" differs from "porewater pH", the latter of which we define here as an in-
situ measure of porewater $H^+$ concentration in soil/weathering profiles. The difference between the two pH measurements is
often not fully known for a given system but could lead to a misunderstanding of soil conditions if the two measurements are
15   directly compared. Agricultural soils are one of the targeted loci for application of the "Enhanced Rock Weathering" (ERW),
a technique aimed at counteracting increasing anthropogenic carbon dioxide from burning fossil fuels, and an increase in pH
is thought to be one of key advantages of ERW as this can mitigating soil acidification and secure crop yields. As a result,
fully evaluating the biogeochemical and agronomic consequences of ERW approaches requires accurate simulation of both
soil pH ($pH_s$) and porewater pH ($pH_{pw}$). This paper presents an updated version of the reactive transport code SCEPTER
20   (Soil Cycles of Elements simulator for Predicting TERrestrial regulation of greenhouse gases), which enables simulation of
bulk soil pH measurement in the laboratory in addition to porewater pH as measured in the field along with a more
comprehensive representation of cation exchange with solid-phase constituents of bulk soil. We first describe the
implementation of cation exchange in the SCEPTER model, then introduce conceptual modelling frameworks enabling the
calculation of bulk $pH_s$. The validity of the model is examined through comparison of model results with soil pH
25   measurements from mesocosm experiments of maize production with crushed basalt amendments. Finally, illustrative
example simulations are shown demonstrating that a difference between $pH_s$ and $pH_{pw}$ can lead to significantly different
estimates of carbon capture by ERW for a given targeted pH in cropland systems.

# 1 Introduction

30  Continuous harvesting and excess use of nitrogen fertilizers commonly leads to acidification of agricultural soils, which may lead to soil degradation and food insecurity over the coming century (Kopittke et al., 2019). The addition of alkalinity to soils — traditionally through liming, the application of ground, relatively soluble (mostly carbonate) rock/mineral powder to soils (e.g., McLean, 1983; Thomas Sims, 1996; Rengel, 2003; Goulding, 2016) — is a widely utilized remedy to manage soil pH and stabilize crop yields. Addition of alkalinity to soil (including liming practice) has recently attracted attention because

35  it can also sequester atmospheric $CO_2$ (e.g., Hamilton et al., 2007; Swoboda et al., 2022), an action that is urgently needed to help meet the climate targets delineated by the Intergovernmental Panel on Climate Change (IPCC, 2006, 2018). Indeed, Enhanced Rock Weathering (ERW) — the application of finely ground carbonate/silicate rock powder to soils — is one of a number of suggested schemes for actively removing anthropogenic $CO_2$ from the atmosphere at scale (e.g., Rau et al., 2007; Köhler et al., 2010; Taylor et al., 2016; Beerling et al., 2020; Vakilifard et al., 2021; Swoboda et al., 2022; Zhang et al.,

40  2022; Kanzaki et al., 2023). In particular, applying basalt rock powder onto croplands/hinterlands has been suggested to be one of the most economically and ecologically promising $CO_2$ removal schemes given the relatively low toxicity in basalt leachates, sustainable availability of basalt rocks, and a range of potential co-benefits (e.g., Strefler et al., 2018; Beerling et al., 2020; Goll et al., 2021).

The pH change induced by addition of basalt powder is central to the ERW scheme because the resultant pH must be

45  optimal for crop growth (e.g., Fernández and Hoeft, 2009), and the application rate of basalt feedstock will thus scale with the magnitude of desired pH increase (e.g., Kelland et al., 2020; Kantzas et al., 2022; Zhang et al., 2022; Dietzen and Rosing, 2023). However, interpretation of pH in soil is not always straightforward because two different types of pH measurements may potentially be regarded as a pH reference for evaluating soil acidity. One is referred to as "soil pH" — defined here as $pH_s$ — which measures $H^+$ residing in bulk soil samples that is in practice measured in the laboratory as the

50  pH of liquid extractants (deionized water or $KCl/CaCl_2$ solution) of bulk soil samples taken from the field. The other is "porewater pH" — defined here as $pH_{pw}$ — which measures in-situ $H^+$ concentrations in porewater flowing through or remaining in the soil/weathering profiles (e.g., Geibe et al., 2006; Steiner et al., 2018). In agricultural/agronomic situations it is most common to measure $pH_s$ (e.g., Thomas, 1996), while models that simulate biogeochemical reactions and transport within soils, including dissolution of basalt during ERW, typically calculate $pH_{pw}$ (e.g., Kelland et al., 2020; Kanzaki et al.,

55  2022). Potential differences between these distinct tracers of soil acidity are poorly explored, and in many cases the heterogeneous continuum that exists between dissolved $H^+$ in pore fluids and exchangeable $H^+$ on soil cation exchange sites is not discussed (cf., Nielsen et al., 2017).

Here, we present a newly developed numerical scheme in an attempt to fill in this technical and knowledge gap and to develop a more mechanistic understanding of the difference between porewater pH and bulk soil pH. A numerical reactive

60   transport model — SCEPTER (Soil Cycles of Elements simulator for Predicting TERrestrial regulation of greenhouse gases; Kanzaki et al., 2022) — has been updated to enable simulations of soil pH ($pH_s$) along with porewater pH ($pH_{pw}$). We first present the essential updates to the SCEPTER code (Section 2.1) and then describe potential modelling frameworks for simulating soil pH with the updated version of the model (Section 2.2). Then, the validity of the model is examined through comparison between simulated and observed soil pH for a set of mesocosm experiments amending a natural soil/maize

65   system with crushed basalt (Section 3). We then discuss the implications of the difference between porewater and soil pH for ERW and the associated impacts on soil acidity by showing example simulations in which basalt feedstock is added to cropland soil using either $pH_s$ or $pH_{pw}$ as a target pH for ERW deployment (Section 4). Finally, we provide a summary of conclusions and touch briefly on future directions for model development (Section 5).

## 2 Model description

70   The SCEPTER model simulates reactions and transport of solid, aqueous, and gas species within soil, including dissolution/precipitation of minerals, three-phase biogeochemical reaction, bio-mixing and uplift/erosion of solid phases, advective and diffusive transport of aqueous species, and gaseous diffusion (Kanzaki et al., 2022). The model is developed for simulating not only natural weathering processes, but also ERW with its specific features that allow explicit bio-mixing of soil including tilling by farmers, addition of solid materials on the topsoil and tracking of particle size distributions which

75   facilitates surface area calculation for individual solid species. This updated version of the code (v1.0) adds several new functions/options to the previously published version (v0.9; Kanzaki et al., 2022). Among them, implementation of cation exchange is essential to the simulation of soil pH as the uptake of cations by solid phase exchangers is a determinant factor of the exchangeable acidity and nutrient cycling in soils. We first describe the implementation of cation exchange in SCEPTER (Section 2.1) and then frameworks for simulation of soil pH using the current version of the code (Section 2.2).

80   ### 2.1 Cation exchange in SCEPTER

The current version of SCEPTER allows cation exchange involving $H^+$, $Na^+$, $K^+$, $Ca^{2+}$, $Mg^{2+}$ and $Al^{3+}$ on specified solid species. Cation exchange reactions are assumed to be in equilibrium, and their fundamental reactions can be written as reactions among surfaces of solid phase exchangers and the cations:

$$Z_\varsigma X(\theta)^- + \varsigma^{Z_\varsigma +} \Leftrightarrow \varsigma\text{-}X(\theta)_{Z_\varsigma} \qquad\qquad , (1)$$

85   where $Z_\varsigma$ is the valence number of cation $\varsigma$, $X(\theta)^-$ denotes exchangeable surface sites of solid phase exchanger $\theta$ and $\varsigma$-$X(\theta)_{Z_\varsigma}$ represents the cation $\varsigma$ adsorbed onto exchangeable sites of $\theta$. Eq. (1) should be regarded as a half reaction because the surface fraction of $X(\theta)^-$ must be very small compared to the surface sites where net local charge is zero because of adsorption under natural conditions (Appelo, 1994). Physically relevant net cation exchange can then be written as a combination of Eq. (1) for a given cation and Eq. (1) for a reference/competing cation so that the combined reaction equation

90 does not have $X(\theta)^-$. As a reference cation, $Na^+$ and $Cs^+$ have been considered (e.g., Appelo, 1994; Steefel et al., 2002; Steefel, 2009). Here, we use $H^+$ as a reference competing agent and then the net exchange reaction can be given as:

$$(1/Z_\varsigma)\varsigma^{Z_\varsigma+} + \text{H-X}(\theta) \Leftrightarrow (1/Z_\varsigma)\varsigma\text{-X}(\theta)_{Z_\varsigma} + H^+ \tag{2}$$

The equilibrium constant for Eq. (2) can be defined as follows:

$$K'_{\varsigma\backslash\text{H},\theta} = \frac{f^{1/Z_\varsigma}(\varsigma\text{-X}(\theta)_{Z_\varsigma})[H^+]}{f(\text{H-X}(\theta))[\varsigma^{Z_\varsigma+}]^{1/Z_\varsigma}} \tag{3}$$

95 where $f(i)$ denotes the charge-equivalent fraction of surface species $i$, and $[j]$ represents the concentration of aqueous species $j$ (mol L$^{-1}$). The apparent equilibrium constant $K'_{\varsigma\backslash\text{H},\theta}$ can vary as a result of surface fraction $X(\theta)^-$ and we adopt the formulation by Appelo (1994):

$$K'_{\varsigma\backslash\text{H},\theta} = \eta_{\text{H},\theta} K_{\varsigma\backslash\text{H},\theta} \tag{4}$$

Here, $K_{\varsigma\backslash\text{H},\theta}$ is the intrinsic equilibrium constant and $\eta_{\text{H},\theta}$ is formulated as a function of $1 - f(\text{H-X}(\theta))$ assuming that $f(X(\theta)^-)$ is

100 proportional to $1 - f(\text{H-X}(\theta))$ (Appelo, 1994):

$$\log \eta_{\text{H},\theta} = -\alpha_\theta \{1 - f(\text{H-X}(\theta))\} \tag{5}$$

where $\alpha_\theta$ is assumed to be 3.4 by default.

The solution for the fraction of surface species can be obtained by considering mass balance at the exchangeable sites for each exchanger:

105 $$CEC_\theta = \sum_\varsigma Z_\varsigma \langle \varsigma\text{-X}(\theta)_{Z_\varsigma} \rangle \tag{6}$$

where $CEC_\theta$ is the cation exchange capacity of exchanger $\theta$ (eq g$^{-1}$) and $\langle i \rangle$ is the concentration of surface species $i$ (mol g$^{-1}$). By definition,

$$f(\varsigma\text{-X}(\theta)_{Z_\varsigma}) \equiv \frac{Z_\varsigma \langle \varsigma\text{-X}(\theta)_{Z_\varsigma} \rangle}{CEC_\theta} \tag{7}$$

Therefore, Eq. (6) can be alternatively written as

110 $$1 = \sum_\varsigma f(\varsigma\text{-X}(\theta)_{Z_\varsigma}) \tag{8}$$

Further, with Eqs. (3) and (4), Eq. (8) can be transformed into

$$1 = f(\text{H-X}(\theta)) + \sum_{\varsigma \neq \text{H}} \left( \frac{\eta_{\text{H},\theta} K_{\varsigma\backslash\text{H},\theta} f(\text{H-X}(\theta))}{[H^+]} \right)^{Z_\varsigma} [\varsigma^{Z_\varsigma+}] \tag{9}$$

Eq. (9) is solved for $f(\text{H-X}(\theta))$ once given a porewater chemistry and thermodynamic constants for exchange reactions (Table 1). Once $f(\text{H-X}(\theta))$ is obtained fractions of all surface species can be calculated using Eqs. (3)-(5).

115 In the previous version of SCEPTER, the key variables for tracking aqueous species are the total concentrations for individual dissolved elements (denoted as $c_\varsigma$ for dissolved element $\varsigma$). In the updated model, the tracked independent

variables have been changed to the concentrations of free dissolved species (except for Si, for which $H_4SiO_4$ concentration is tracked), denoted as $c_\varsigma^1$. These $c_\varsigma$ and $c_\varsigma^1$ are related to one another by the following equation (Kanzaki et al., 2022):

$$c_\varsigma = c_\varsigma^1 + c_\varsigma^1 \sum_{i=2}^{n_\varsigma} K_{\varsigma,i} [\mathrm{H^+}]^{\gamma_{\varsigma,i,\mathrm{p}}} \prod_{\varsigma' \neq \varsigma}^{n_{\mathrm{aq}}} (c_{\varsigma'}^1)^{\gamma_{\varsigma,i,\varsigma'}} \prod_{\varepsilon}^{n_{\mathrm{gas}}} (p_\varepsilon)^{\gamma_{\varsigma,i,\varepsilon}} \qquad , (10)$$

120    where the second term on the right-hand side is the sum of the concentrations of dissolved element $\varsigma$ other than $c_\varsigma^1$, denoted as the $i$-th species of dissolved element $\varsigma$ where $i \neq 1$, with $K_{\varsigma,i}$ being the thermodynamic constant for production of $i$-th aqueous species of dissolved element $\varsigma$, $\gamma_{\varsigma,i,\mathrm{p}}$, $\gamma_{\varsigma,i,\varsigma'}$ and $\gamma_{\varsigma,i,\varepsilon}$ the stoichiometry of $H^+$, dissolved element $\varsigma'$ and gas species $\varepsilon$, respectively, in the reaction that produces $i$-th aqueous species of $\varsigma$, $p_\varepsilon$ the partial pressure (atm) of gas species $\varepsilon$, and $n_{\mathrm{aq}}$ and $n_{\mathrm{gas}}$ the total numbers of independent aqueous and gas species, respectively (see Kanzaki et al. (2022) for more details). This

125    modification of tracked independent variables (from $c_\varsigma$ to $c_\varsigma^1$) facilitates our implementation of cation exchange.

In accord with the implementation of cation exchange as well as modification of independent variables to track for aqueous species described above, the governing equation for aqueous species has been updated to:

$$\frac{\partial \phi \sigma \ell \beta_\varsigma^{\mathrm{aq}} c_\varsigma^1}{\partial t} + \frac{\partial B_\varsigma^{\mathrm{ads}} c_\varsigma^1}{\partial t} = -\frac{\partial \phi \sigma \ell v \beta_\varsigma^{\mathrm{aq}} c_\varsigma^1}{\partial z} + \frac{\partial}{\partial z}\left( \phi \sigma \ell \, \tau_{\mathrm{aq}} D_\varsigma \frac{\partial \beta_\varsigma^{\mathrm{aq}} c_\varsigma^1}{\partial z} \right) + \sum_\theta^{n_{\mathrm{sld}}} \gamma_{\theta,\varsigma} R_\theta + \sum_\kappa^{n_{\mathrm{xrxn}}} \gamma_{\kappa,\varsigma} R_\kappa$$

$$+ \frac{\partial w B_\varsigma^{\mathrm{ads}} c_\varsigma^1}{\partial z} - B_\varsigma^{\mathrm{ads}} c_\varsigma^1 \int_0^{z_{\mathrm{ml}}} E_\theta(z,z') dz' + \int_0^{z_{\mathrm{ml}}} B_\varsigma^{\mathrm{ads}} c_\varsigma^1(z') E_\theta(z',z) dz' \qquad , (11)$$

130    where $\beta_\varsigma^{\mathrm{aq}}$ and $B_\varsigma^{\mathrm{ads}}$ ($m^{-3}$ L) are the factors to convert $c_\varsigma^1$ to $c_\varsigma$ and to the total concentration of element $\varsigma$ adsorbed onto solid phases, respectively, $t$ is time (yr), $z$ is the depth of weathering profile (m), $\phi$ is the porosity, $\sigma$ is the water saturation ratio, $\ell$ is a unit conversion factor ($10^3$ L $m^{-3}$), $v$ is the porewater advection rate (m $yr^{-1}$), $\tau_{\mathrm{aq}}$ is the tortuosity factor for solute diffusion in porewater, $D_\varsigma$ is the diffusion coefficient of dissolved element $\varsigma$ ($m^2$ $yr^{-1}$), $n_{\mathrm{sld}}$ is the total number of simulated solid species, $\gamma_{\theta,\varsigma}$ is the mole amount of $\varsigma$ released upon dissolution of 1 mole of mineral $\theta$, $R_\theta$ is the net dissolution rate of

135    solid species $\theta$ (mol $m^{-3}$ $yr^{-1}$), $n_{\mathrm{xrxn}}$ is the total number of extra reactions, $\gamma_{\kappa,\varsigma}$ is the stoichiometry of $\varsigma$ production in $\kappa$-th extra reaction, $R_\kappa$ denotes the rate of $\kappa$-th extra reaction (mol $m^{-3}$ $yr^{-1}$), $w$ is the advection rate of solid phases (m $yr^{-1}$), $E_\theta(z,z')$ is the rate of particle transfer between locations at $z$ and $z'$ by bio-mixing ($m^{-1}$ $yr^{-1}$) and $z_{\mathrm{ml}}$ is the mixed layer depth (m) within which bio-mixing occurs. The left-hand side of Eq. (11) denotes the time change rate of dissolved and adsorbed forms of $\varsigma$. The first and second terms on the right-hand side show the advective and diffusive transport rates of dissolved

140    forms of $\varsigma$, respectively, the third and fourth terms net supply of $\varsigma$ through dissolution/precipitation of solid phases and extra biogeochemical reactions, respectively, and the rest of the terms the advective transport (fifth term) and bio-mixing (sixth and seventh terms) rates of adsorbed forms of $\varsigma$ along with solid phase exchangers (see Kanzaki et al. (2022) for further details on the reactions and transport schemes implemented in SCEPTER). The values of $\beta_\varsigma^{\mathrm{aq}}$ and $B_\varsigma^{\mathrm{ads}}$ can be calculated from Eqs. (10) and (3)-(9), respectively:

145
$$\beta_\varsigma^{\mathrm{aq}} \equiv \frac{c_\varsigma}{c_\varsigma^1} = 1 + \sum_{i=2}^{n_\varsigma} K_{\varsigma,i}[\mathrm{H^+}]^{\gamma_{\varsigma,i,\mathrm{p}}} \prod_{\varsigma' \neq \varsigma}^{n_{\mathrm{aq}}} (c_{\varsigma'}^1)^{\gamma_{\varsigma,i,\varsigma'}} \prod_{\varepsilon}^{n_{\mathrm{gas}}} (p_\varepsilon)^{\gamma_{\varsigma,i,\varepsilon}}$$
, (12)

$$B_\varsigma^{\mathrm{ads}} \equiv \begin{cases} \dfrac{1}{c_\varsigma^1} \sum_\theta m_\theta M_\theta \langle \varsigma\text{-}\mathrm{X}(\theta)_{Z_\varsigma} \rangle = \sum_\theta \dfrac{m_\theta M_\theta CEC_\theta}{Z_\varsigma} \left( \dfrac{\eta_{\mathrm{H},\theta} K_{\varsigma \backslash \mathrm{H},\theta} f(\mathrm{H\text{-}X}(\theta))}{[\mathrm{H^+}]} \right)^{Z_\varsigma} & (\varsigma \in \{\mathrm{Na, K, Ca, Mg, Al}\}) \\ 0 & (\text{else}) \end{cases}$$
, (13)

where $m_\theta$ and $M_\theta$ are the concentration (mol m$^{-3}$) and molar weight (g mol$^{-1}$) of solid species $\theta$, respectively.

The updated version of the governing equation for aqueous species (Eq. 11) is solved together with those for solid and gaseous species as described by Kanzaki et al. (2022), except that the calculation of surface speciation via cation exchange is
150 additionally included during each update of porewater pH and aqueous speciation. Default thermodynamic constants and capacities of cation exchange are tabulated in Tables 1 and 2, respectively. Cation exchange can be switched on and off by specifying so in the `switches.in` input file. One can also modify the parameters for cation exchange using another input file `cec.in`. Instructions for running example simulations from this paper are given in *Code Availability*.

## 2.2 Soil pH simulation by SCEPTER

155 In silico calculation of bulk soil pH (pH$_\mathrm{s}$) imitates the procedure to measure soil pH in the laboratory: sampling bulk soils, mixing them with an extractant solution (e.g., deionized water or KCl/CaCl$_2$ solution) at a given soil/solution ratio (e.g., 1:1 or 1:5 g/ml), bringing the mixtures to a short-term equilibrium, and measuring extractant solution pH (e.g., McLean, 1983; Thomas, 1996; Jones, 1999; Kissel and Sonon, 2008). Even "soil buffer pH" — a measure of resistance of bulk soil to a pH change — can be calculated in silico using the same procedure but with a specified buffer solution (e.g., Thomas Sims, 1996;
160 Sikora, 2006) instead of the extractant solutions implemented for measuring bulk agronomic pH. Our procedure for calculating soil (buffer) pH can be summarized as follows:

1. A "field simulation" is run, which can be fed by field observations.
2. Data from the field run are retrieved at a given model field depth and/or averaged over a given depth interval, including output for:

165
    a. Concentrations and cation exchange properties (e.g., Tables 1 and 2) of unextractable solid phases (e.g., silicates)

    b. Concentrations of exchangeable (i.e., dissolved plus adsorbed) cations and anions

    c. Concentrations of cations and anions in extractable solid phases (e.g., salts)

3. Boundary conditions for a "laboratory simulation" are determined based on Step 2 in order to realize a hypothetical
170 laboratory "beaker/flask", where a bulk soil sample and an extractant solution (deionized water or electrolyte solution) are mixed homogeneously at a given soil/solution ratio.

    a. Concentrations of unextractable solid species obtained in Step 2 are given as the initial/boundary concentrations in an input file (`parentrock.in`) for the laboratory run. Those solid species are not

allowed to dissolve/precipitate in the laboratory run because of the short duration for soil pH

175    measurements (e.g., Thomas, 1996), realized by setting their rate constants at zero in an input file

(`kinspc.in`). Meanwhile cation exchange properties of the unextractable solid species are assumed to be

the same as those in the field run (these can be specified in the corresponding input file `cec.in`).

b.    Exchangeable/extractable cations and anions are added to the calculation domain of laboratory

"beaker/flask" as an appropriate combination of oxides and salts whose complete dissolution is allowed

180    (Table 3). Note that dissolved inorganic carbon (DIC) is an exception and is instead added as the most

labile class of organic matter (Table 3). The amount of solid species added is calculated as $z_{lab}(1 -$

$\phi_{lab})C_\varsigma M_\theta/\gamma_{\theta,\varsigma}$ (g m$^{-2}$) where $z_{lab}$ (m) is the depth of the beaker/flask filled with the mixture of soil sample

and solution, $\phi_{lab}$ is the volume ratio of fluid against solid phases calculated as $\phi_{lab} = \psi(\rho^{-1} + \psi)^{-1}$ with the

soil/solution ratio used in the laboratory ($\psi$, g cm$^{-3}$) and bulk soil particle density ($\rho$, g cm$^{-3}$) observed in

185    the in-silico field, $C_\varsigma$ is the concentration of exchangeable/extractable cation/anion $\varsigma$ (mol m$^{-3}$), $M_\theta$ is the

molar weight of the added solid species $\theta$ (g mol$^{-1}$) and $\gamma_{\theta,\varsigma}$ is the mole of $\varsigma$ contained in 1 mole of $\theta$. When

soil pH is measured in the mixture of bulk soil sample and an electrolyte solution, corresponding salt is

additionally added in the amount of $z_{lab}\phi_{lab}\ell c_\Theta M_\theta/\gamma_{\theta,\Theta}$ (g m$^{-2}$) where $c_\Theta$ and $\gamma_{\theta,\Theta}$ are the solution

concentration (mol L$^{-1}$) of electrolyte $\Theta$ and mole of electrolyte $\Theta$ in 1 mole of salt $\theta$, respectively (e.g., $c_\Theta$

190    = 0.01 mol L$^{-1}$ and $\gamma_{\theta,\Theta} = 1$ if $\theta = CaCl_2$ else $\gamma_{\theta,\Theta} = 0$ when $\Theta = CaCl_2$). When simulating soil buffer pH, the

salt added corresponding to the electrolyte described above must be replaced by a series of solid phases

corresponding to solute ingredients according to the recipe of the buffer solution (e.g., Table 4 for a buffer

solution by Sikora, 2006), enabling at the same time tracking of corresponding aqueous species with

relevant aqueous diffusion coefficients and association/dissociation thermodynamics (e.g., Tables 5 and 6,

195    respectively, for Sikora buffer solution). These constituents are added to the beaker/flask only once at the

beginning of a laboratory simulation.

c.    The beaker/flask domain of the laboratory simulation is assumed to be a closed system for solid, aqueous,

and gaseous species, except for the addition of solid/salt phases at the beginning of the run described in

Step 3b above, i.e., no advective transport for solid, aqueous and gaseous phases and no diffusive in- and

200    out-fluxes of aqueous and gaseous species at the boundaries (specified in input files `frame.in` and

`switches.in`).

4.    The laboratory simulation is run for long enough to achieve equilibrium.

Figure 1 schematically illustrates the procedure described above, from running a field simulation and sampling data from the

205    in-silico field to soil pH measurement in the laboratory. As implied by the schematic (e.g., compare aqueous compositions

illustrated for "porewater" in Step 3 and extractant solution in Step 4 of Fig. 1), porewater and soil pH can differ. Indeed,

under the conditions considered in our analysis a significant offset between $pH_s$ and $pH_{pw}$ is confirmed to be a general phenomenon, as discussed below. In the next section, we discuss the validity of our approach toward simulating $pH_s$ with SCEPTER using observed soil and porewater pH data from a mesocosm experiment along with other observed soil chemical

210 characteristics. After examining the validity of the model (Section 3) we present examples of the model application to ERW and discuss how the difference between porewater and soil pH can potentially lead to significant differences in the prediction of the amount of basalt feedstock required to achieve a given agronomic target pH in agricultural soils (Section 4).

## 3 Model validation

In order to validate our approach toward calculating bulk agronomic soil pH in the reaction-transport model, we compare a
215 series of soil pH simulations fed by field simulation with observed boundary conditions to results from a mesocosm experiment. The mesocosm has been monitored since July 2022, and the field simulation is constrained from detailed measurements conducted in August 2022 (Table 7) as boundary conditions (Table 8). The field simulation is simplified as much as possible as the focus of this paper is simulation of soil pH (see Kanzaki et al., 2022, for some additional examples of field simulations fitted to observations). A detailed description of the mesocosm setup can be found in Chiaravalloti et al.
220 (2023). Its tracked solid species are limited to soil organic matter and a "bulk" solid-phase species (i.e., a hypothetical species representing the solid phases other than soil OM dumped together as a whole) treated as two cation exchangers; tracked aqueous species include base cations (Na, K, Ca, Mg), $NO_3$ and Cl; and $CO_2$ gas. The tracked solid species (i.e., soil OM and "bulk" species) are assumed to have the same values for thermodynamic parameters for cation exchange except that they have different CEC values (120 and 3.176 cmol kg$^{-1}$, respectively) with their average constrained from the observed
225 bulk soil CEC (8.9 cmol kg$^{-1}$). Measured porewater composition at 15 cm depth is used as the upper boundary condition for aqueous base cations in the field simulation so that simulated porewater composition at 15 cm depth is consistent with observations (Fig. 2a). Aqueous $NO_3$ is added as $NH_4NO_3$ fertilizer at the upper boundary in the field simulation at the same rate of total N supply as the Urea-$NH_4$-$NO_3$ fertilizer applied to the mesocosm (24.210 gN m$^{-2}$ yr$^{-1}$). Upper aqueous Cl concentration takes a fitted value (Table 8) so that the simulated porewater pH at 15 cm depth is consistent with observations
230 (Fig. 3a). Soil OM input is fixed at the value (Table 8) with which simulated average OM concentration over the top 15 cm is consistent with observations (4.9 wt%). See Table 8 for more details on the boundary conditions for the field simulation.

Soil samples from the mesocosm experiments were homogenized from the top 15 cm of soil (dried at 60°C overnight and sieved at 2mm), and measured soil pH values and electrical conductivity values were obtained from a series of solutions: in deionized water at soil/solution ratios of 1:5, 1:2, 1:1 and 1:0.5 (g/cm$^3$); and in 0.0025, 0.005 and 0.01 M $CaCl_2$ solution at
235 1:1 soil/solution ratio (g/cm$^3$). The pH for each soil/solution slurry was measured with a Thermo Scientific Orion ROSS Ultra pH/ATC Triode paired with a Thermo Scientific Orion STARA2215 Orion Star A221 Portable pH Meter (ThermoFisher Scientific, Massachusetts). Electrical conductivity was measured by placing a few drops of the liquid from

the soil/solution slurry on a HOBO U24 Conductivity Logger (U24-002-C) (Onset Computer Corporation, Massachusetts). We also measured buffer pH from a soil split using the method and recipe developed by Sikora (2006).

240    Soil pH simulations are conducted based on averaged data over top 15 cm of bulk soil from the field simulation described above, supplemented with the mesocosm observations according to the procedure described in Section 2.2. A series of soil pH values is calculated: in deionized water at soil/solution ratios of 1:5, 1:2, 1:1 and 1:0.5 (g/cm³); and in 0.0025, 0.005 and 0.01 M CaCl₂ solution at 1:1 soil/solution ratio (g/cm³) following Miller and Kissel (2010). We also calculate soil buffer pH where bulk soil over the upper 15 cm, deionized water, and Sikora buffer solution are mixed in 1:1:1

245    ratio (g:cm³:cm³) following the recipe by Sikora (2006). The observation shows significant amounts of extractable $NO_3$ and Cl (Table 7), which probably exist as some forms of salts and are not explicitly simulated in the field run. Therefore, those extractable anions are added to the laboratory runs so that all major extractable/exchangeable elements measured in the mesocosm samples are consistent between the laboratory simulation and observations.

    The simulated field run shows abundances of exchangeable cations over the top 15 cm that match well with

250    observations (Fig. 2b) with the optimized thermodynamic parameters for cation exchange (Table 8). Simulated soil buffer pH is also consistent with observed buffer pH for the topsoil of the mesocosm (Fig. 3a). Although soil buffer pH was measured using Sikora buffer, we can confirm that the model can effectively reproduce the relationship between Sikora buffer pH and neutralized acid measured by the Sikora method (Fig. 3b). Therefore, in-silico measurement of soil buffer pH should be directly comparable with the observational data. Simulated soil pH varies as a function of dilution by deionized

255    water and/or the concentration of CaCl₂ in solution, a trend especially obvious when soil pH is plotted against electrical conductivity as shown in Fig. 4a (in-silico electrical conductivity is calculated from ionic strength assuming a conversion factor of 0.016 dS m⁻¹ mol⁻¹ L from Ponnamperuma et al., 1966; cf. Alva et al., 1991). This trend is also consistent with observations (Table 9 and Fig. 4a). The difference of soil pH in deionized water from that in 0.01 M CaCl₂ solution at the same soil/solution ratio of 1:1 (g/cm³), defined as $\Delta pH_{1:1}$ (Muller and Kissel, 2010), is also consistent with the mesocosm

260    observations as well as the trend observed for U.S. soils by Miller and Kissel (2020) (Fig. 4b). Overall, with optimized thermodynamics of cation exchange the model can very closely reproduce observed porewater and soil (buffer) pH results for both our mesocosm experiments and previously published data.

## 4 Example ERW application

To illustrate the potential importance of distinguishing between $pH_s$ and $pH_{pw}$ and modelling both accurately, we present

265    example simulations in which alkalinity addition to soils through ERW is limited by an assumed target pH and compare cases in which the target value is assumed to be $pH_s$ with an equivalent ensemble in which it is assumed to be $pH_{pw}$. Here, we consider another simple soil system: tracked solid species include the "bulk" and SOM species; aqueous species are $Ca^{2+}$ and $NO_3$; and $CO_2$ is the only tracked gaseous species. Boundary conditions are those of an arbitrarily chosen field site from the Midwest U.S. (Table 10) and the cation exchange thermodynamics, soil respiration, and base saturation are

270 correspondingly constrained from the observation at the site. More specifically, the system is tuned up with varying $Ca^{2+}$
concentration at the upper boundary and thermodynamic coefficients for Ca-H exchange and OM input to soil (3 unknowns)
until the system satisfies the observed soil pH, exchangeable acidity and SOM wt% (6.058, 20.980 %CEC, 2.052 wt%,
respectively; 3 observed knowns) at steady state. Mechanistically, the non-zero value of $Ca^{2+}$ concentration at the upper
boundary can be taken to reflect the net result of historical liming at the site. We then add a "glassy basalt" solid species

275 iteratively to meet a range of target pH values (6.2, 6.5 and 6.8) after one year of basalt application and use the model to
estimate the rate of basalt application required to achieve a given target pH value. We run two ensembles, one with $pH_s$ as
the operative target pH and one with $pH_{pw}$ as the target, allowing us to compare the estimated basalt feedstock application
required to reach identical target pH when using $pH_s$ or $pH_{pw}$ as an index. Soil pH is calculated in a mixture of top 15 cm
bulk soil and deionized water at 1:1 $g/cm^3$ ratio. The observed data used for the initial spin/tune-up is from: Fick and

280 Hijmans (2017) for temperature, Wang et al. (2019) for soil moisture, Reitz et al. (2017) for runoff, Poggio et al. (2021) for
soil pH and OM, Walkinshaw et al. (2022) for cation exchange capacity, Pan et al. (2021) for nitrification rate, and ISRIC
(2022) for base saturation. Basalt application simulations are all conducted as re-starts from the end of the same spin/tune-up
described above, where glassy basalt is applied and mixed with bulk soil via tilling during initial 0.005 yr (~2 days). For
glassy basalt, we use the kinetic law formulated by Brantley et al. (2008) and the thermodynamic calculation method used by

285 Aradóttir et al. (2012) and Pollyea and Rimstidt (2017) and assumed a log normal distribution centered at 10 µm with 0.2 log
unit standard deviation for the initial particle size distribution and the chemical composition in the caption of Table 10. See
Table 10 for additional details on model boundary conditions.

Depending on the pH reference (i.e., either soil pH, $pH_s$, or porewater pH, $pH_{pw}$), required amount of basalt is
significantly different at any of the target pH values examined here (Fig. 5). Comparison of soil and porewater pH (Figs. 6

290 and 7) shows that variation in soil pH is more limited compared to that of porewater pH because soil pH largely reflects
exchangeable acidity, which can more effectively buffer input of alkalinity compared to acidity of porewater although the
total exchangeable acidity is dependent on the cation exchange capacity and initial base saturation of soil. Porewater pH is
lower than soil pH at relatively low alkalinity input (e.g., at earlier time after basalt deployment and/or at deep depths, Figs.
6 and 7), given that in-situ porewater pH reflects higher soil $pCO_2$ while soil pH has lower re-equilibrated $pCO_2$ from

295 conserved DIC because of dilution by deionized water. With higher alkalinity input (e.g., at later time after basalt
deployment and/or at shallower depths, Figs. 6 and 7), porewater pH is higher than soil pH because soil pH has a maximum
value set by the cation exchange capacity at 100% base saturation. In general, using $pH_{pw}$ as the index target requires higher
alkalinity input via basalt dissolution for a given target pH value. Though only meant to be illustrative, the example
simulations shown here clearly demonstrate the importance of distinguishing between soil and porewater pH in numerical

300 frameworks for representing soil pH regulation.

## 5 Conclusions

We update the SCEPTER model (v1.0) to simulate the mechanics of cation exchange, and an associated, newly developed framework that enables calculation of soil pH in silico. By comparing to observational measurements from mesocosm
305 experiments, we demonstrate that soil pH simulation in SCEPTER can accurately reproduce systematic variations in observed porewater pH, soil pH and soil buffer pH, so long as a field simulation can validated by accessory soil chemistry. We also presented example simulations which focus on the application of the model to estimation of required basalt for agricultural soils to reach different target pH values through ERW. We observe significant differences in response to an alkalinity input via basalt dissolution between porewater and soil pH, with important implications for diagnosing agricultural
310 soils with respect to an optimal basalt deployment rate/style through ERW and managing crop yields. Future model developments include an extension of cation exchange to a more generalized suite of sorption reactions, e.g., implementation of anion (e.g., $PO_4$) adsorption onto oxides (e.g., van der Zee and van Riemsdijk, 1988; McGechan and Lewis, 2002) as well as nutrient uptake by plants, to comprehensively predict nutrient cycling and productivity in cropland soils in parallel with anthropogenic alkalinity modification and $CO_2$ removal through enhanced rock weathering.

315 **Code availability**

The source codes of the model are available at GitHub (https://github.com/cdr-laboratory/SCEPTER) under the GNU General Public License v3.0. The specific version of the model used in this paper is tagged as "v1.0" and has been assigned a doi (https://doi.org/10.5281/zenodo.8078586). A readme file on the web provides the instructions for executing the simulations.

320 **Author contributions**

YK and CTR designed and implemented the model with significant contributions from the other authors. IC obtained mesocosm data. SZ and YK compiled and filtered soil data from the literature. All authors contributed to the experimental design and YK conducted the experiments and analysed the results. All authors contributed to the writing of the paper.

**Competing interests**

325 The authors declare no competing interests.

## References

Alva, A. K., Sumner, M. E. and Miller, W. P.: Relationship between ionic strength and electrical conductivity for soil solutions, Soil Sci., 152(4), 239-242, https://doi.org/10.1097/00010694-199110000-00001, 1991.

Appelo, C. A. J.: Cation and proton exchange, pH variations, and carbonate reactions in a freshening aquifer, Water Resour.
330    Res., 30(10), 2793-2805, https://doi.org/10.1029/94WR01048, 1994.

Aradóttir, E. S. P., Sonnenthal, E. L. and Jónsson, H.: Development and evaluation of a thermodynamic dataset for phases of interest in $CO_2$ mineral sequestration in basaltic rocks, Chem. Geol., 304, 26-38, https://doi.org/10.1016/j.chemgeo.2012.01.031, 2012.

Beerling, D. J., Kantzas, E. P., Lomas, M. R., Wade, P., Eufrasio, R. M., Renforth, P., Sarkar, B., Andrews, M. G., James, R.
335    H., Pearce, C. R., Mercure, J.-F., Pollitt, H., Holden, P. B., Edwards, N. R., Khanna, M., Koh, L., Quegan, S., Pidgeon, N. F., Janssens, I. A., Hansen, J., and Banwart, S. A.: Potential for large-scale $CO_2$ removal via enhanced rock weathering with croplands, Nature, 583, 242–248, https://doi.org/10.1038/s41586-020-2448-9, 2020.

Brantley, S. L., Kubicki, J. D., and White, A. F.: Kinetics of Water-Rock Interaction, Springer, 2008.

Chiaravalloti, I., Theunissen, N., Zhang, S., Wang, J., Sun, F., Ahmed, A. A., Pihlap, E., Reinhard, C. T., and Planavsky, N.
340    J.: Mitigation of soil nitrous oxide emissions during maize production with basalt amendments, Front. Clim., 5, https://doi.org/10.3389/fclim.2023.120343, 2023.

Fernández, F. G. and Hoeft, R. G.: Managing soil pH and crop nutrients, In: Illinois Agronomy Handbook, 24, 91-112, 2009.

Fick, S. E. and Hijmans, R. J.: WorldClim 2: new 1km spatial resolution climate surfaces for global land areas, Int. J. Climatol., 37(12): 4302-4315, 2017.

345    Geibe, C. E., Danielsson, R., van Hees, P. A. and Lundström, U. S.: Comparison of soil solution chemistry sampled by centrifugation, two types of suction lysimeters and zero-tension lysimeters, Appl. Geochem., 21(12), 2096-2111, https://doi.org/10.1016/j.apgeochem.2006.07.010, 2006.

Goldberg, R. N., Kishore, N. and Lennen, R. M.: Thermodynamic quantities for the ionization reactions of buffers, J. Phys. Chem. Ref. Data, 31(2), 231-370, https://doi.org/10.1063/1.1416902, 2002.

350    Goll, D. S., Ciais, P., Amann, T., Buermann, W., Chang, J., Eker, S., Hartmann, J., Janssens, I., Li, W., Obersteiner, M., Penuelas, J., Tanaka, K., and Vicca, S: Potential $CO_2$ removal from enhanced weathering by ecosystem responses to powdered rock, Nat. Geosci, 14, 545–549, https://doi.org/10.1038/s41561-021-00798-x, 2021.

Goulding, K. W. T.: Soil acidification and the importance of liming agricultural soils with particular reference to the United Kingdom, Soil Use Manage., 32(3), 390-399, https://doi.org/10.1111/sum.12270, 2016.

355    Hamilton, S. K., Kurzman, A. L., Arango, C., Jin, L. and Robertson, G. P.: Evidence for carbon sequestration by agricultural liming. Global Biogeochem. Cycles, 21, GB2021, https://doi.org/10.1029/2006GB002738, 2007.

IPCC: 2006 IPCC Guidelines for National Greenhouse Gas Inventories, IPCC, 2006.

IPCC: Global Warming of 1.5°C, IPCC, 2018.

ISRIC: WISE Soil Property Databases, available at: https://www.isric.org/explore/wise-databases, last access: 2022.

360  Jones, Jr, J. B. (ed.): Soil Analysis Handbook of Reference Methods, CRC press, 1999.

Kantzas, E. P., Val Martin, M., Lomas, M. R., Eufrasio, R. M., Renforth, P., Lewis, A. L., Taylor, L. L., Mecure, J. F., Pollitt, H., Vercoulen, P. V. and Vakilifard, N.: Substantial carbon drawdown potential from enhanced rock weathering in the United Kingdom. Nat. Geosci., 15(5), 382-389, https://doi.org/10.1038/s41561-022-00925-2, 2022.

Kanzaki, Y., Planavsky, N. J. and Reinhard, C. T.: New estimates of the storage permanence and ocean co-benefits of
365  enhanced rock weathering, PNAS Nexus, 2(4), pgad059, https://doi.org/10.1093/pnasnexus/pgad059, 2023.

Kanzaki, Y., Zhang, S., Planavsky, N. J. and Reinhard, C. T.: Soil Cycles of Elements simulator for Predicting TERrestrial regulation of greenhouse gases: SCEPTER v0.9, Geosci. Model Dev., 15, 4959–4990, https://doi.org/10.5194/gmd-15-4959-2022, 2022.

Kelland, M. E., Wade, P. W., Lewis, A. L., Taylor, L. L., Sarkar, B., Andrews, M. G., Lomas, M. R., Cotton, T. A., Kemp,
370  S. J., James, R. H. and Pearce, C. R.: Increased yield and $CO_2$ sequestration potential with the $C_4$ cereal Sorghum bicolor cultivated in basaltic rock dust-amended agricultural soil, Global Change Biology, 26(6), 3658-3676, https://doi.org/10.1111/gcb.15089, 2020.

Kissel, D. E. and Sonon, L. S.: Soil Test Handbook for Georgia, University of Georgia College of Agricultural and Environmental Sciences, Athens, GA, 2008.

375  Kopittke, P. M., Menzies, N. W., Wang, P., McKenna, B. A. and Lombi, E.: Soil and the intensification of agriculture for global food security, Environ. Int., 132, 105078, https://doi.org/10.1016/j.envint.2019.105078, 2019.

Köhler, P., Hartmann, J., and Wolf-Gladrow, D. A.: Geoengineering potential of artificially enhanced silicate weathering of olivine, Proc. Natl. Acad. Sci. U. S. A., 107, 20228– 20233, https://doi.org/10.1073/pnas.1000545107, 2010.

La-Scalea, M. A., Menezes, C. M. S. and Ferreira, E. I.: Molecular volume calculation using AM1 semi-empirical method
380  toward diffusion coefficients and electrophoretic mobility estimates in aqueous solution, J. Mol. Struct.: THEOCHEM, 730(1-3), 111-120, https://doi.org/10.1016/j.theochem.2005.05.030, 2005.

Li, Y. -H. and Gregory, S.: Diffusion of ions in sea water and in deep-sea sediments, Geochim. Cosmochim. Acta., 38, 703– 714, https://doi.org/10.1016/0016-7037(74)90145-8, 1974.

Likhachev, E. R.: Dependence of water viscosity on temperature and pressure, Tech. Phys., 48(4), 514-515,
385  https://doi.org/10.1134/1.1568496, 2003.

McGechan, M. B. and Lewis, D. R.: SW—soil and water: sorption of phosphorus by soil, part 1: principles, equations and models, Biosyst. Eng., 82(1), 1-24, https://doi.org/10.1006/bioe.2002.0054, 2002.

McLean, E. O.: Soil pH and lime requirement, In: Methods of Soil Analysis: Part 2 Chemical and Microbiological Properties, 9 (ed. by A. L. Page), 199-224, https://doi.org/10.2134/agronmonogr9.2.2ed.c12, 1983.

390  Miller, R. O. and Kissel, D. E.: Comparison of soil pH methods on soils of North America, Soil Sci. Soc. Am. J., 74(1), 310-316, https://doi.org/10.2136/sssaj2008.0047, 2010.

Nielsen, K. E., Irizar, A., Nielsen, L. P., Kristiansen, S. M., Damgaard, C., Holmstrup, M., Petersen, A. R. and Strandberg, M.: In situ measurements reveal extremely low pH in soil, Soil Biol. Biochem., 115, 63-65, https://doi.org/10.1016/j.soilbio.2017.08.003, 2017.

395    Othmer, D. F. and Thakar, M. S.: Correlating diffusion coefficient in liquids, Ind. Eng. Chem., 45(3), 589-593, https://doi.org/10.1021/ie50519a036, 1953.

Pan, B., Lam, S. K., Wang, E., Mosier, A. and Chen, D.: New approach for predicting nitrification and its fraction of $N_2O$ emissions in global terrestrial ecosystems, Environ. Res. Lett., 16(3), 034053, https://doi.org/10.1088/1748-9326/abe4f5, 2021.

400    Parfitt, R. L., Giltrap, D. J. and Whitton, J. S.: Contribution of organic matter and clay minerals to the cation exchange capacity of soils, Commun. Soil Sci. Plant Anal., 26(9-10), 1343-1355, https://doi.org/10.1080/00103629509369376, 1995.

Parkhurst, D. L. and Appelo, C. A. J.: Description of input and examples for PHREEQC version 3: a computer program for speciation, batch-reaction, one-dimensional transport, and inverse geochemical calculations, U. S. Geological Survey, 405    https://doi.org/10.3133/tm6A43, 2013.

Poggio, L., De Sousa, L. M., Batjes, N. H., Heuvelink, G., Kempen, B., Ribeiro, E. and Rossiter, D.: SoilGrids 2.0: producing soil information for the globe with quantified spatial uncertainty, Soil, 7(1), 217-240, https://doi.org/10.5194/soil-7-217-2021, 2021.

Pollyea, R. M. and Rimstidt, J. D.: Rate equations for modeling carbon dioxide sequestration in basalt, Appl. Geochem., 81, 410    53-62, https://doi.org/10.1016/j.apgeochem.2017.03.020, 2017.

Ponnamperuma, F. N., Tianco, E. M. and Loy, T. A.: Ionic strengths of the solutions of flooded soils and other natural aqueous solutions from specific conductance, Soil Sci., 102(6), 408-413, https://doi.org/10.1097/00010694-196612000-00009, 1966.

Rau, G. H., Knauss, K. G., Langer, W. H., and Caldeira, K.: Reducing energy-related $CO_2$ emissions using accelerated 415    weathering of limestone, Energy, 32, 1471–1477, https://doi.org/10.1016/j.energy.2006.10.011, 2007.

Reitz, M., Sanford, W. E., Senay, G. B. and Cazenas, J.: Annual estimates of recharge, quick-flow runoff, and evapotranspiration for the contiguous US using empirical regression equations. J. Am. Water Resour. Assoc., 53(4), 961-983, https://doi.org/10.1111/1752-1688.12546, 2017.

Rengel, Z., ed.: Handbook of Soil Acidity, CRC Press, https://doi.org/10.1201/9780203912317, 2003.

420    Robie, R. A. Hemingway, B. S., and Fisher, J. R.: Thermodynamic properties of minerals and related substances at 298.15 K and 1 bar ($10^5$ pascals) pressure and at higher temperatures, U. S. Geological Survey, 1978.

Schulz, H. D. and Zabel, M.: Marine Geochemistry, Springer, https://doi.org/10.1007/3-540-32144-6, 2006.

Sikora, F. J.: A buffer that mimics the SMP buffer for determining lime requirement of soil, Soil Sci. Soc. Am. J., 70(2), https://doi.org/10.2136/sssaj2005.0164, 474-486, 2006.

425    Steefel, C. I.: CrunchFlow Software for Modeling Multicomponent Reactive Flow and Transport USER'S MANUAL, 2009.

Steefel, C. I., Carroll, S., Zhao, P. and Roberts, S.: Cesium migration in Hanford sediment: a multisite cation exchange model based on laboratory transport experiments, J. Contam. Hydrol., 67(1-4), 219-246, https://doi.org/10.1016/S0169-7722(03)00033-0, 2003.

Steiner, Z., Lazar, B., Erez, J. and Turchyn, A. V.: Comparing Rhizon samplers and centrifugation for pore-water separation
430    in studies of the marine carbonate system in sediments, Limnol. Oceanogr.-Meth., 16(12), 828-839, https://doi.org/10.1002/lom3.10286, 2018.

Strefler, J., Amann, T., Bauer, N., Kriegler, E., and Hartmann, J.: Potential and costs of carbon dioxide removal by enhanced weathering of rocks, Environ. Res. Lett., 13, 034010, https://doi.org/10.1088/1748-9326/aaa9c4, 2018.

Swoboda, P., Döring, T. F. and Hamer, M.: Remineralizing soils? The agricultural usage of silicate rock powders: A review,
435    Sci. Total Environ., 807, 150976, https://doi.org/10.1016/j.scitotenv.2021.150976, 2022.

Taylor, L. L., Quirk, J., Thorley, R. M. S., Kharecha, P. A., Hansen, J., Ridgwell, A., Lomas, M. R., Banwart, S. A., and Beerling, D. J.: Enhanced weathering strategies for stabilizing climate and averting ocean acidification, Nat. Clim. Change, 6, 402–406, https://doi.org/10.1038/NCLIMATE2882, 2016.

Thomas, G. W.: Soil pH and soil acidity, in: Methods of Soil Analysis: Part 3 Chemical Methods, 5 (eds. by D. L. Sparks, A.
440    L. Page, P. A. Helmke, R. H. Loeppert, P. N. Soltanpour, M. A. Tabatabai, C. T. Johnston, M. E. Sumner), 475-490, https://doi.org/10.2136/sssabookser5.3.c16, 1996.

Thomas Sims, J.: Lime requirement, in: Methods of Soil Analysis: Part 3 Chemical Methods, 5 (eds. by D. L. Sparks, A. L. Page, P. A. Helmke, R. H. Loeppert, P. N. Soltanpour, M. A. Tabatabai, C. T. Johnston, M. E. Sumner), 491-515, https://doi.org/10.2136/sssabookser5.3.c17, 1996.

445    van der Zee, S. E. and van Riemsdijk, W. H.: Model for long-term phosphate reaction kinetics in soil, J. Environ. Qual., 17, 35-41, https://doi.org/10.2134/jeq1988.00472425001700010005x, 1988.

Vakilifard, N., Kantzas, E. P., Edwards, N. R., Holden, P. B. and Beerling, D. J.: The role of enhanced rock weathering deployment with agriculture in limiting future warming and protecting coral reefs, Environ. Res. Lett., 16(9), 094005, https://doi.org/10.1088/1748-9326/ac1818, 2021.

450    Walkinshaw, M., O'Geen, A. T., Beaudette, D. E.: Soil Properties, California Soil Resource Lab, casoilresource.lawr.ucdavis.edu/soil-properties/, 2022.

Wang, Y., Mao, J., Jin, M., Hoffman, F. M., Shi, X., Wullschleger, S. D. and Dai, Y.: Development of observation-based global multilayer soil moisture products for 1970 to 2016, Earth Syst. Sci. Data, 13(9), 4385-4405, https://doi.org/10.5194/essd-13-4385-2021, 2021.

455    Zhang, S., Planavsky, N. J., Katchinoff, J., Raymond, P. A., Kanzaki, Y., Reershemius, T. and Reinhard, C. T.: River chemistry constraints on the carbon capture potential of surficial enhanced rock weathering, Limnol. Oceanogr., 67. S148-S157, https://doi.org/10.1002/lno.12244, 2022.

Table 1. Default thermodynamic data of cation exchange [a].

| Reaction | log $K_{\varsigma \backslash H}$ | Ref./note [b] |
|---|---|---|
| $Na^+ + H\text{-}X = Na\text{-}X + H^+$ | −5.9 | 1 |
| $K^+ + H\text{-}X = K\text{-}X + H^+$ | −4.8 | 2 |
| $Ca^{2+} + 2H\text{-}X = Ca\text{-}X_2 + 2H^+$ | −10.47 | 2 |
| $Mg^{2+} + 2H\text{-}X = Mg\text{-}X_2 + 2H^+$ | −10.786 | 2 |
| $Al^{3+} + 3H\text{-}X = Al\text{-}X_3 + 3H^+$ | −16.47 | 3 |

[a] The same set of thermodynamic data is assumed for any sold phase exchanger. Therefore, the notation of solid phase $\theta$ used in Section 2 is dropped in this table.

[b] (1) From modelled value at zero $f$(H-X) in Appelo (1994). (2) Calculated from log $K_{\varsigma \backslash Na}$ = 1.1, 0.507, and 0.665 for $\varsigma$ = K, Mg, and Ca, respectively, from Appelo (1994). (3) Calculated from log $K_{Al \backslash Na}$ = 0.41 from phreeqc.dat available in PHREEQC v.3 (Parkhurst and Appelo, 2013).

Table 2. Default cation exchange capacity of solid species [a].

| ID | Name | $CEC_\theta$ [ceq kg$^{-1}$] | Ref./note [c] |
|---|---|---|---|
| ka | kaolinite | 16.2 | 1 |
| nabd, kbd, mgbd, cabd | Na-, K-, Mg-, Ca-beidellite | 70 | 2 |
| g1, g2, g3 | SOM [b] Class 1, 2, 3 | 330 | 2 |

[a] Those solid species that are not listed here are assumed to have zero cation exchange capacity.

[b] SOM — soil organic matter.

[c] (1) Beerling et al. (2020). (2) Parfitt et al. (1995).

Table 3. Solid species to be dissolved in laboratory simulations [a].

| ID | Name | Composition | $M_\theta$ [g mol$^{-1}$] | $V_\theta$ [cm$^3$ mol$^{-1}$] | log $K_\theta^{\text{ref}}$ [(mol L$^{-1}$)$^x$][b] | $\Delta H_\theta$ [kJ mol$^{-1}$] | Ref./ note [c] |
|---|---|---|---|---|---|---|---|
| na2o | Na$_2$O | Na$_2$O | 61.979 | 25.88 | 67.4269 | −351.636 | 1,2 |
| k2o | K$_2$O | K$_2$O | 94.195 | 40.38 | 84.0405 | −427.006 | 1,2 |
| mgo | MgO | MgO | 40.304 | 11.248 | 21.3354 | −150.139 | 1,2 |
| cao | CaO | CaO | 56.079 | 16.764 | 32.5761 | −193.832 | 1,2 |
| fe2o | FeO | FeO | 71.846 | 12 | 13.5318 | −106.052 | 1,2 |
| al2o3 | Corundum | Al$_2$O$_3$ | 101.962 | 25.575 | 18.3121 | −258.626 | 1,2 |
| sio2 | SiO$_2$ | SiO$_2$ | 60.085 | 22.688 | -2.71 | 13.97456 | 1,3 |
| caso4 | Anhydrite | CaSO$_4$ | 136.138 | 45.94 | −4.36 | −7.2 | 1,4 |
| nacl | Halite | NaCl | 58.443 | 27.015 | 1.5855 | 3.7405 | 1,2 |
| kcl | Sylvite | KCl | 74.551 | 37.524 | 0.8459 | 17.4347 | 1,2 |
| cacl2 | Hydrophilite | CaCl$_2$ | 110.986 | 50.75 | 11.7916 | −81.4545 | 1,2 |
| naoh | NaOH | NaOH | 39.9971 | 18.778 | - | - | 5 |
| amnt | NH$_4$NO$_3$ | NH$_4$NO$_3$ | 80.043 | 46.402 | - | - | 5 |
| g1 | SOM Class 1 | CH$_2$O | 30 | 20 | - | - | 5 |
| teas | Triethanolamine | C$_6$H$_{15}$NO$_3$ | 149.190 | 132.731 | - | - | 5 |
| ims | Imidazole | C$_3$H$_4$N$_2$ | 68.077 | 55.347 | - | - | 5 |
| mesmh | MES monohydrate | C$_6$H$_{13}$NO$_4$S•H$_2$O | 213.25 | 380.803 | - | - | 5 |
| gac | Acetic acid | CH$_3$COOH | 60.052 | 47.285 | - | - | 5 |

[a] Thermodynamic constants for solid species $\theta$ ($K_\theta$) are calculated as $K_\theta = K_\theta^{\text{ref}} \exp(-\Delta H_\theta (T^{-1} - 298^{-1}) \mathscr{R}^{-1})$ where $T$ is temperature in K and $\mathscr{R}$ is the gas constant in units of kJ mol$^{-1}$ K$^{-1}$ ($\mathscr{R}$ = 8.314×10$^{-3}$ kJ mol$^{-1}$ K$^{-1}$). Solid species listed here are assumed to have decomposition rates that are represented by short turnover time (≤1 year) and do not depend on surface areas but their concentrations (see Kanzaki et al., 2022). Variation in kinetic constants does not affect the soil pH simulations as long as they are run long enough to attain equilibrium.

[b] Units change with $x$ depending on solid species.

[c] (1) $M_\theta$ and $V_\theta$ from Robie et al. (1978). (2) $K_\theta^{\text{ref}}$ and $\Delta H_\theta$ from llnl.dat available in PHREEQC v.3 (Parkhurst and Appelo, 2013). (3) $K_\theta^{\text{ref}}$ and $\Delta H_\theta$ are assumed to be the same as those for amorphous Si. (4) $K_\theta^{\text{ref}}$ and $\Delta H_\theta$ from minteq.v4.dat available in PHREEQC v.3 (Parkhurst and Appelo, 2013). (5) Assumed to be undersaturated unconditionally. $M_\theta$ is calculated from chemical formula and $V_\theta$ is based on $M_\theta$ assuming density of 2.13, 1.725, 1.5, 1.124, 1.23, 0.56, and 1.27 g cm$^{-3}$ for NaOH, NH$_4$NO$_3$, SOM Class 1, triethanolamine, imidazole, MES (2-(N-morpholino)ethanesulfonic acid) monohydrate, and acetic acid, respectively.

Table 4. Sikora buffer composition [a].

| Solute | $c_\Theta$ [mol L$^{-1}$] |
|---|---|
| Triethanolamine | 0.0696 |
| Imidazole | 0.0137 |
| MES | 0.0314 |
| Acetic acid | 0.0893 |
| KCl | 2.00 |
| NaOH | 0.058 |

[a] From Sikora (2006) except that NaOH concentration is modified so that mixture of Sikora buffer with deionized water at 1:1 volume ratio has a pH of 7.5.

Table 5. Diffusion coefficients for aqueous species in Sikora buffer.

| Species | $a$ | $b$ | Ref./note [a] |
|---|---|---|---|
| Triethanolamine | 177.3 | - | 1,2 |
| Imidazole | 75.3 | - | 1,2 |
| MES | 380.803 | - | 1,3 |
| Acetate | 0.0251 | 21.57 | 4,5 |
| Cl | 0.0494 | 18.95 | 4,6 |

[a] (1) Diffusion coefficient (m$^2$ yr$^{-1}$) is calculated as $D = 0.4415(\mu_w^{-1.1}a^{0.6})^{-1}$ where $\mu_w$ is the water viscosity (mPa s) and $a$ is the molar volume of solute (cm$^3$ mol$^{-1}$) (Othmer and Thakar, 1953; La-Scalea et al., 2005). The water viscosity $\mu_w$ is calculated as $\mu_w = 0.024152\exp(4.7428(T - 139.86)^{-1}\mathscr{R}^{-1})$ where $\mathscr{R} = 8.314 \times 10^{-3}$ kJ mol$^{-1}$ K$^{-1}$ and $T$ is temperature in K, according to Likhachev (2003). (2) $a$ from La-Scalea et al. (2005). (3) $a$ is assumed to be equivalent to that of MES monohydrate. (4) Diffusion coefficient (m$^2$ yr$^{-1}$) is calculated as $D = a \times \exp(-b(T^{-1} - 288^{-1})\mathscr{R}^{-1})$ where $a$ is the pre-exponential factor (m$^2$ yr$^{-1}$) and $b$ is the apparent activation energy (kJ mol$^{-1}$). (5) $a$ and $b$ from Schulz and Zabel (2006). (6) $a$ and $b$ from Li and Gregory (1974).

Table 6. Thermodynamic data for aqueous species in Sikora buffer [a].

| Reaction [b] | log $K_{aq}^{ref}$ [(mol L$^{-1}$)$^x$] [c] | $\Delta H_{aq}$ [kJ mol$^{-1}$] | Ref./note [d] |
|---|---|---|---|
| TEA + H$^+$ = TEA(H)$^+$ | 8.09 | −33.6 | 1 |
| IM + H$^+$ = IM(H)$^+$ | 7.10 | −36.64 | 1 |
| MES(−H)$^-$ + H$^+$ = MES | 6.18 | −14.8 | 1 |
| AcO$^-$ + H$^+$ = AcOH | 4.48 | 0.41 | 1 |
| Cl$^-$ + H$^+$ = HCl | −0.67 | 0 | 2 |
| Cl$^-$ + Na$^+$ = NaCl | −0.777 | 5.21326 | 2 |
| Cl$^-$ + K$^+$ = KCl | −1.4946 | 14.1963 | 2 |
| Cl$^-$ + Mg$^{2+}$ = MgCl$^+$ | −0.1349 | −0.58576 | 2 |
| Cl$^-$ + Ca$^{2+}$ = CaCl$^+$ | −0.6956 | 2.02087 | 2 |
| Cl$^-$ + Fe$^{2+}$ = FeCl$^+$ | −0.1605 | 3.02503 | 2 |
| Cl$^-$ + Fe$^{3+}$ = FeCl$^{2+}$ | −0.8108 | 36.6421 | 2 |

[a] Thermodynamic constant ($K_{aq}$) is calculated as $K_{aq} = K_{aq}^{ref} \exp(-\Delta H_{aq}(T^{-1}-298^{-1})\mathscr{R}^{-1})$ where $\mathscr{R} = 8.314 \times 10^{-3}$ kJ mol$^{-1}$ K$^{-1}$ and $T$ is temperature in K.

[b] TEA — Triethanolamine; TEA(H)$^+$ — H$^+$-associated triethanolamine; IM — Imidazole; IM(H)$^+$ — H$^+$-associated imidazole; MES — 2-(N-morpholino)ethanesulfonic acid; MES(−H)$^-$ — H$^+$-dissociated MES; AcO$^-$ — Acetate anion; AcOH — Acetic acid.

[c] Units change with $x$ depending on reaction.

[d] (1) $K_{aq}^{ref}$ from Sikora (2006) and $\Delta H_{aq}$ from Goldberg et al. (2002). (2) From llnl.dat available in PHREEQC v3.0 (Parkhurst and Appelo, 2013).

Table 7. Compositional data measured for mesocosm soil sample.

| Element | Porewater at 15 cm [mol L$^{-1}$] | Extractable/exchangeable [ppm] | Exchangeable fraction [%CEC] |
|---|---|---|---|
| Na | 9.5948×10$^{-5}$ | 13 | 0.6 |
| K | 7.1579×10$^{-4}$ | 57 | 1.6 |
| Mg | 1.9203×10$^{-4}$ | 179 | 16.8 |
| Ca | 1.3624×10$^{-3}$ | 996 | 56 |
| Al | 2.2872×10$^{-9}$ | - | - |
| NO$_3$-N | - | 120 | - |
| Cl | - | 1062 | - |

Table 8. Boundary conditions for mesocosm simulations.

| Parameter [a] | Field | Laboratory |
|---|---|---|
| Solid species [b] | inrt, amnt, g2 | inrt, amnt, g1, g2, cao, mgo, k2o, na2o, kcl, (cacl2)[c], (teas, ims, mesmh, gac, naoh)[d] |
| Aqueous species | Na, K, Ca, Mg, $NO_3$, Cl | Na, K, Ca, Mg, $NO_3$, Cl, (TEA, IM, MES, AcO)[d,e] |
| Gas species | $CO_2$ | $CO_2$ |
| OM [gC m$^{-2}$ yr$^{-1}$] [f] | 1338 | 0 |
| $NH_4NO_3$ [gN m$^{-2}$ yr$^{-1}$] | 69.172 | 0 |
| $J_\theta$ [g m$^{-2}$ yr$^{-1}$] | 0 | Sections 2.2 and 3 |
| $N$ | 30 | 30 |
| $z_{tot}$ [m] | 0.5 | 0.05 |
| $w$ [mm yr$^{-1}$] | 1 | 0 |
| Bio-mixing ($z_{ml}$ [m]) | Fickian (0.25) | No |
| log $r_H$ [m] | −5 | −5 |
| $q$ [m yr$^{-1}$] | 0.55 | 0 |
| $\sigma_0$ | 0.22 | 1 |
| $z_{sat}$ [m] | 1000 | 1000 |
| $CEC_{inrt}$ [ceq kg$^{-1}$] [f,g] | 3.176 | 3.176 |
| $CEC_{g2}$ [ceq kg$^{-1}$] [f,g] | 120 | 120 |
| $c^0_{Cl}$ [mmol L$^{-1}$] [f,h] | $2.68\times10^{-4}$ | - |
| log $K_{Na\backslash H}$ [f,i] | −4.027 | −4.027 |
| log $K_{K\backslash H}$ [f,i] | −4.474 | −4.474 |
| log $K_{Ca\backslash H}$ [f,i] | −9.032 | −9.032 |
| log $K_{Mg\backslash H}$ [f,i] | −8.704 | −8.704 |
| $\alpha$ [f,i] | 1.3 | 1.3 |

[a] $J_\theta$ — addition rate of solid species $\theta$ at the upper boundary of the calculation domain, $N$ — number of grid cells in the calculation domain, $z_{tot}$ — total depth of the calculation domain, $w$ — uplift/erosion rate, $z_{ml}$ — mixed layer depth, $r_H$ — hydraulic radius of particles for solid phases, $q$ — annual runoff, $\sigma_0$ — water saturation ratio at the surface, $z_{sat}$ — water table depth, $CEC_\theta$ — cation exchange capacity for solid species $\theta$, $c^0_{Cl}$ — concentration of Cl at the surface, $K_{\varsigma\backslash H}$ — intrinsic thermodynamic constant for $\varsigma$-H exchange ($\varsigma$ = Na, K, Mg, and Ca), $\alpha_\theta$ — coefficient to describe surface charge effect on cation exchange thermodynamics for solid species $\theta$ (Section 2.1; Appelo, 1994).

[b] Only IDs of solid species are denoted. inrt — "bulk" species, amnt — $NH_4NO_3$, g1 — SOM Class 1 (most labile class), g2 — SOM Class 2 (second most labile class), na2o— $Na_2O$, k2o — $K_2O$, mgo — MgO, cao — CaO, kcl — KCl, cacl2 — $CaCl_2$, teas — Triethanolamine, ims — Imidazole, mesmh — MES (2-(N-morpholino)ethanesulfonic acid) monohydrate, gac — Acetic acid, naoh — NaOH.

[c] Added only when simulating soil pH in $CaCl_2$ solution.

[d] Added only when simulating soil buffer pH by Sikora (2006).

[e] Some of aqueous species in Sikora buffer are abbreviated. TEA — Triethanolamine, IM — Imidazole, MES — 2-(N-morpholino)ethanesulfonic acid, AcO — Acetate anion.

[f] Parameter values optimized to reproduce observation (Section 4).

[g] $CEC_\theta$ = 0 for solid species not listed here.

[h] See Section 3 for base cation concentrations at the upper boundary.

[i] Those values are applied only to bulk and SOM Class 2 species.

Table 9. Porewater and soil (buffer) pH of mesocosm.

| | Porewater pH at 15 cm | Soil pH in deionized water | | | | Soil pH in CaCl$_2$ | | | Buffer pH |
|---|---|---|---|---|---|---|---|---|---|
| | | 1:5 | 1:2 | 1:1 | 1:0.5 | 0.0025 | 0.005 | 0.01 | |
| Observation | 6.68 | 5.81 | 5.54 | 5.42 | 5.48 | 5.31 | 5.29 | 5.24 | 6.28 |
| Simulation | 6.68 | 5.74 | 5.52 | 5.36 | 5.20 | 5.32 | 5.29 | 5.25 | 6.27 |

Table 10. Boundary conditions for ERW simulations.

| Parameter [a] | Field | Laboratory |
|---|---|---|
| Solid species [b] | inrt, amnt, g2, (gbas)[c] | inrt, amnt, g2, (gbas)[c], cao, mgo, k2o, na2o, g1 |
| Aqueous species | Na, K, Ca, Mg, $NO_3$ | Na, K, Ca, Mg, $NO_3$ |
| Gas species | $CO_2$ | $CO_2$ |
| OM [$gC\ m^{-2}\ yr^{-1}$] [d] | 108.35 | 0 |
| Nitrification [$gN\ m^{-2}\ yr^{-1}$] | 1.0059 | 0 |
| $J_\theta$ [$g\ m^{-2}\ yr^{-1}$] | 0 (Depending on target pHs)[c,e] | Sections 2.2 |
| $N$ | 30 | 30 |
| $z_{tot}$ [m] | 0.5 | 0.05 |
| $w$ [$mm\ yr^{-1}$] | 1.013 | 0 |
| Bio-mixing ($z_{ml}$ [m]) [f] | Fickian (0.25) (Inversion (0.25))[c] | No |
| log $r_H$ [m] | −5 (PSD) | −5 |
| $q$ [$m\ yr^{-1}$] | 0.3514 | 0 |
| $\sigma_0$ | 0.2827 | 1 |
| $z_{sat}$ [m] | 1000 | 1000 |
| $CEC$ [$ceq\ kg^{-1}$] | 21.103 | 21.103 |
| $c^0_{Ca}$ [$mmol\ L^{-1}$] [d] | 0.1016 | 0 |
| log $K_{Ca\backslash H}$ [d,g] | −7.448 | −7.448 |

[a] $J_\theta$ — addition rate of solid species $\theta$ at the upper boundary of the calculation domain, $N$ — number of grid cells in the calculation domain, $z_{tot}$ — total depth of the calculation domain, $w$ — uplift/erosion rate, $z_{ml}$ — mixed layer depth, $r_H$ — hydraulic radius of particles for solid phases, $q$ — annual runoff, $\sigma_0$ — water saturation ratio at the surface, $z_{sat}$ — water table depth, $CEC$ — cation exchange capacity assumed for "bulk" species and SOM, $c^0_{Ca}$ — concentration of Ca at the surface, $K_{Ca\backslash H}$ — thermodynamic constant for Ca-H exchange.

[b] Only IDs of solid species are denoted. inrt — "bulk" species, amnt — $NH_4NO_3$, g1 — SOM Class 1 (most labile class), g2 — SOM Class 2 (second most labile class), gbas — glassy basalt, na2o— $Na_2O$, k2o — $K_2O$, mgo — MgO, cao — CaO. Chemical composition of glassy basalt is given by the stoichiometry of $\gamma_{gbas,\varsigma}/\gamma_{gbas,Si}$ = 0.0809, 0.0084, 0.2439, 0.2722, 0.1251, 0.4683, and 1 for $\varsigma$ = Na, K, Ca, Mg, Fe, Al, and Si, respectively.

[c] Only enabled when basalt is applied in a field run or soil pH is simulated for basalt-applied soils.

[d] See Section 4 for the calculation of those parameter values.

[e] See Fig. 5.

[f] Bio-mixing is defined using a modified transition matrix ($K_{\theta,ij}$), which is a discretized form of continuous exchange function $E_\theta$ in Eq. (11) and can be formulated based on transport probability between soil layers $i$ and $j$ ($P_{\theta,ij}$). Inversion mixing in this paper is implemented as $K_{\theta,ij} = \delta z_i P_{inv}/\delta z_j$ if $i = j − 1$ or $i = j + 1$ or $i = n_{ml} + 1 − j$ else 0, where $P_{\theta,ij}$ is assumed to have a phase- and location-independent value $P_{inv} = 0.1\ yr^{-1}$, $\delta z_i$ is the thickness (m) of soil layer $i$ and $n_{ml}$ is the total number of mixed layers. See Kanzaki et al. (2022) for the formulation for Fickian mixing.

[g] Other thermodynamic constants for cation exchange are modified from their default values in Table 1 consistently with the change in $K_{Ca\backslash H}$, e.g., log $K_{\varsigma\backslash H}$ = −4.389, −3.289 and −7.764, for $\varsigma$ = Na, K and Mg, respectively.

Steps 1 & 2. Run field simulation and data sampling of in-silico field
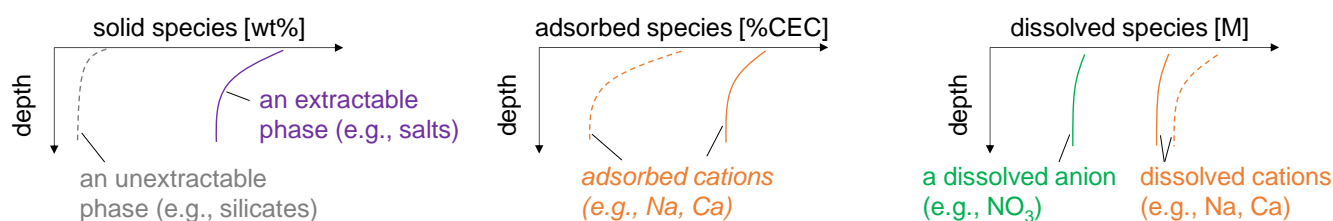
Step 3. Converting sampled field data into inputs of laboratory simulation
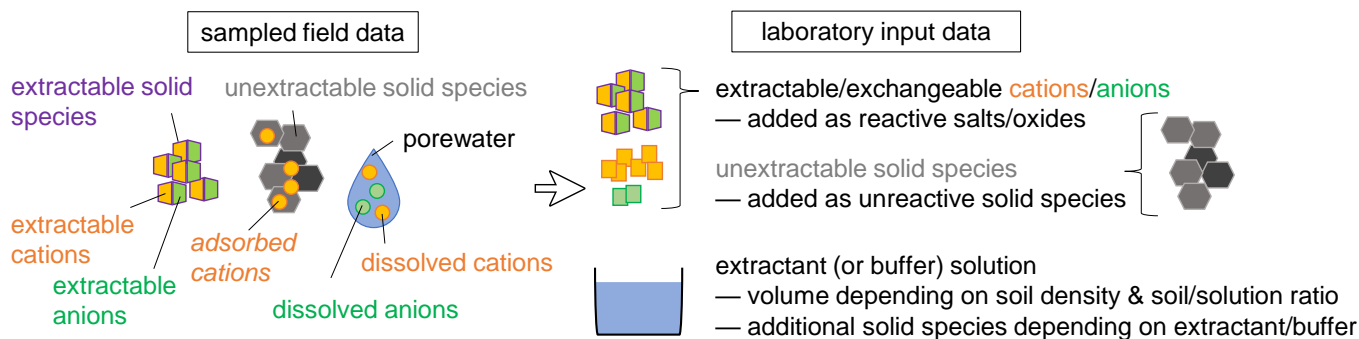
Step 4. Run laboratory simulation to equilibrium
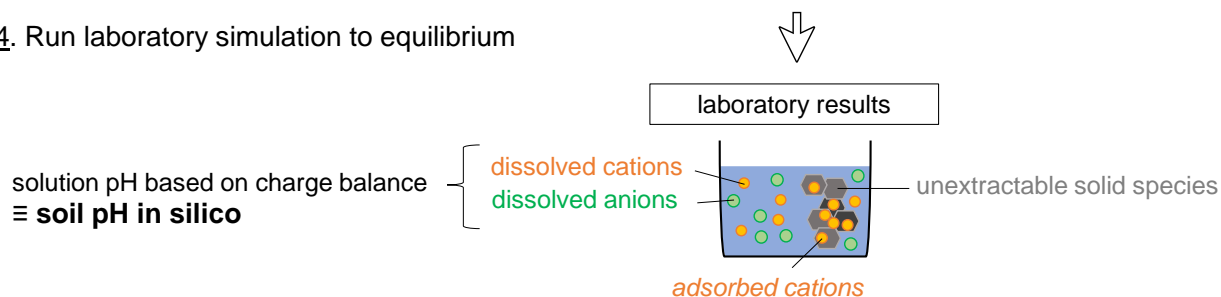
**Figure 1:** Schematic of soil pH calculation procedure. After a field simulation is run to represent a specific field soil (Step 1), in-silico field data are obtained (Step 2) for the concentrations of solid phases (left), adsorbed cations (middle) and dissolved cations and anions (right). In Step 3, sampled in-silico field data are converted to input data for a laboratory simulation in which extractable/exchangeable cations/anions are converted to a combination of salt/oxide phases to be added to the laboratory beaker/flask with additional phases depending on the extractant (or buffer) solution. In Step 4, these added phases are dissolved in the laboratory beaker/flask to reach equilibrium, after which the calculated solution pH corresponds to soil pH (pH$_s$) of the in-silico field soil in Steps 1 and 2.
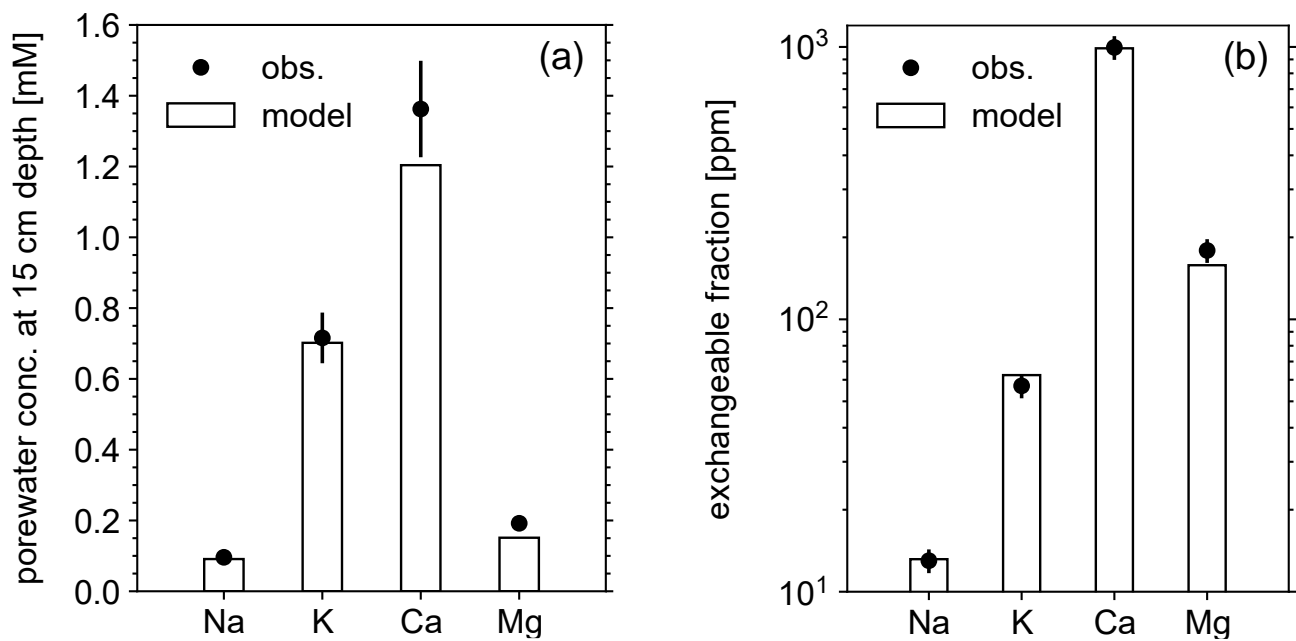
**Figure 2:** Comparison of soil composition between our model simulation and observations from the mesocosm experiments. (a) Porewater chemistry at 15 cm soil depth. (b) Exchangeable fraction of cations over top 15 cm. A uniform 10% error is assumed for observational measurements (see Table 7).
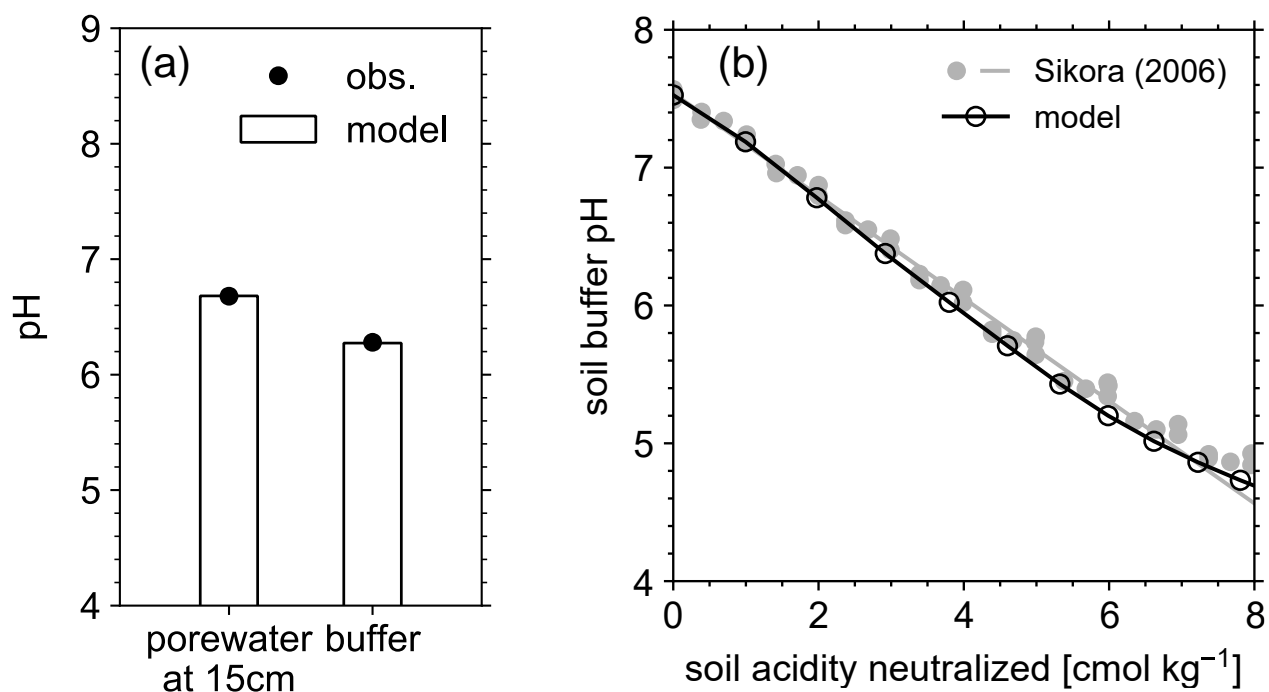
**Figure 3:** (a) Comparison of porewater and soil buffer pH between mesocosm observations and model simulation. (b) Data-model comparison of Sikora buffer pH (2006) as a function of neutralized acidity.
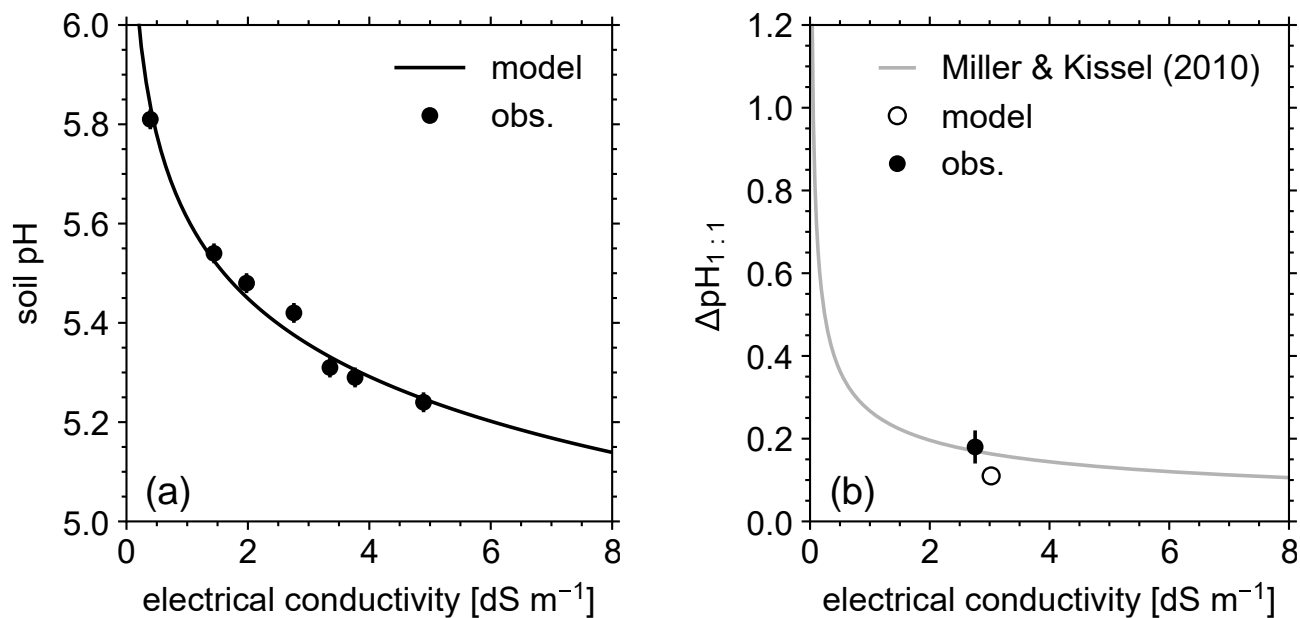
**Figure 4:** (a) Soil pH in deionized water at different soil/solution ratios and in $CaCl_2$ solution at different concentrations plotted against electrical conductivity for both simulations and mesocosm observations. (b) Difference in soil pH at 1:1 soil/solution $g/cm^3$ ratio between in deionized water and 0.01 M $CaCl_2$ solution ($\Delta pH_{1:1}$) plotted against electrical conductivity for both simulated and observed mesocosm, along with the $\Delta pH_{1:1}$ relationship with electrical conductivity derived for U.S. soils by Miller and Kissel (2010). In (a) and (b), measured pH is assumed to have a uniform error of 0.02.
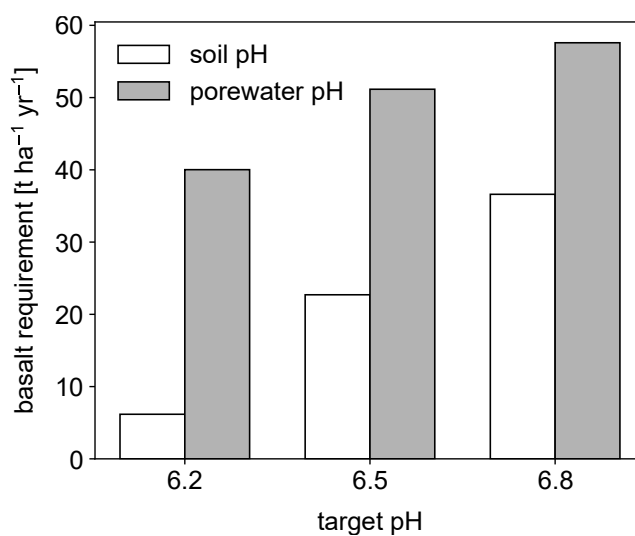
**Figure 5:** Basalt requirements for different target pH values after the first year following feedstock application using either bulk soil or porewater pH as a pH reference value.
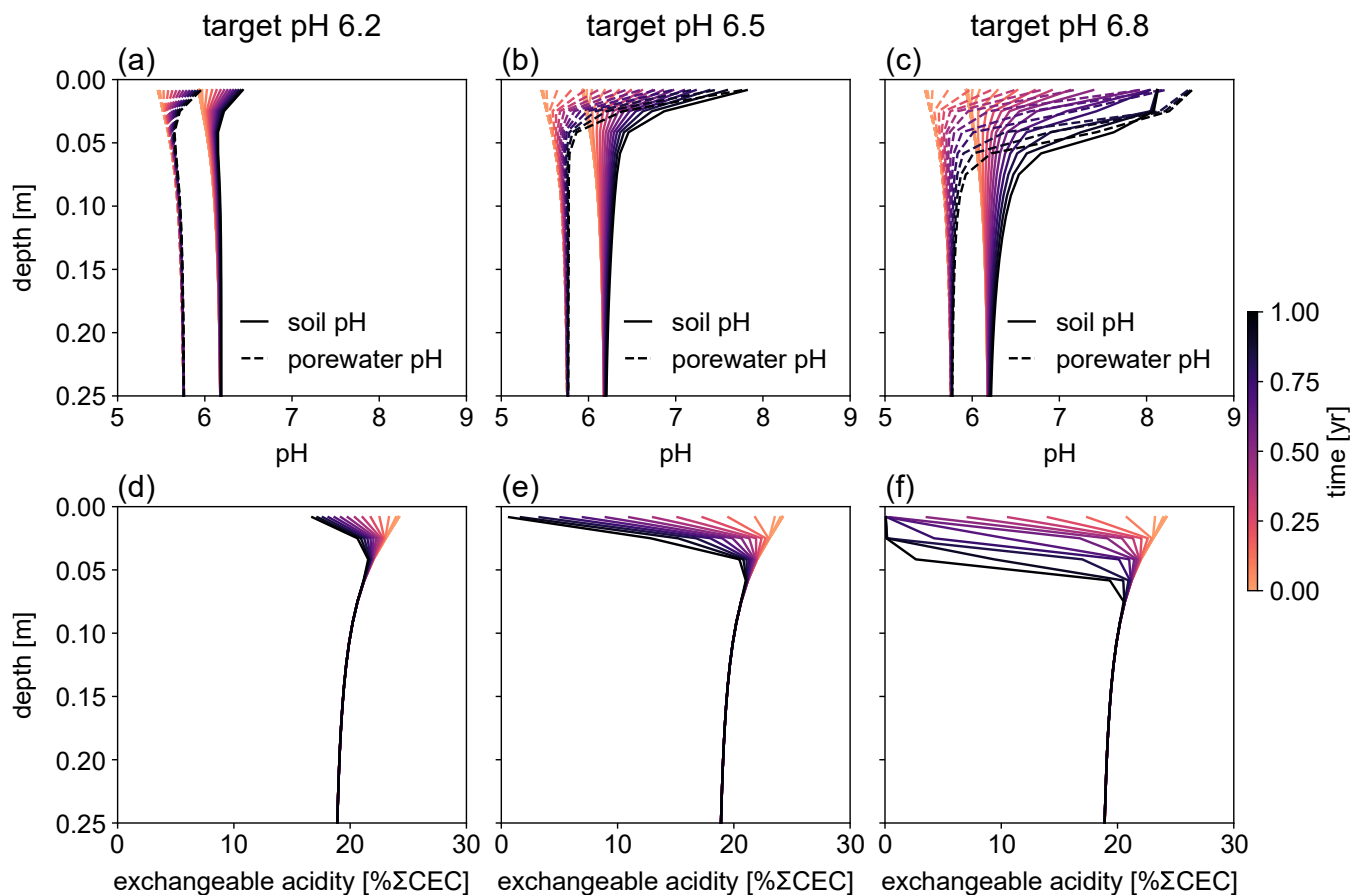
**Figure 6:** Evolution of soil and porewater pH (a-c) and exchangeable acidity (d-f) during the first year following basalt feedstock application at target pH values of of 6.2 (a and d), 6.5 (b and e) and 6.8 (c and f) using soil pH averaged over 0-15 cm as a pH reference.
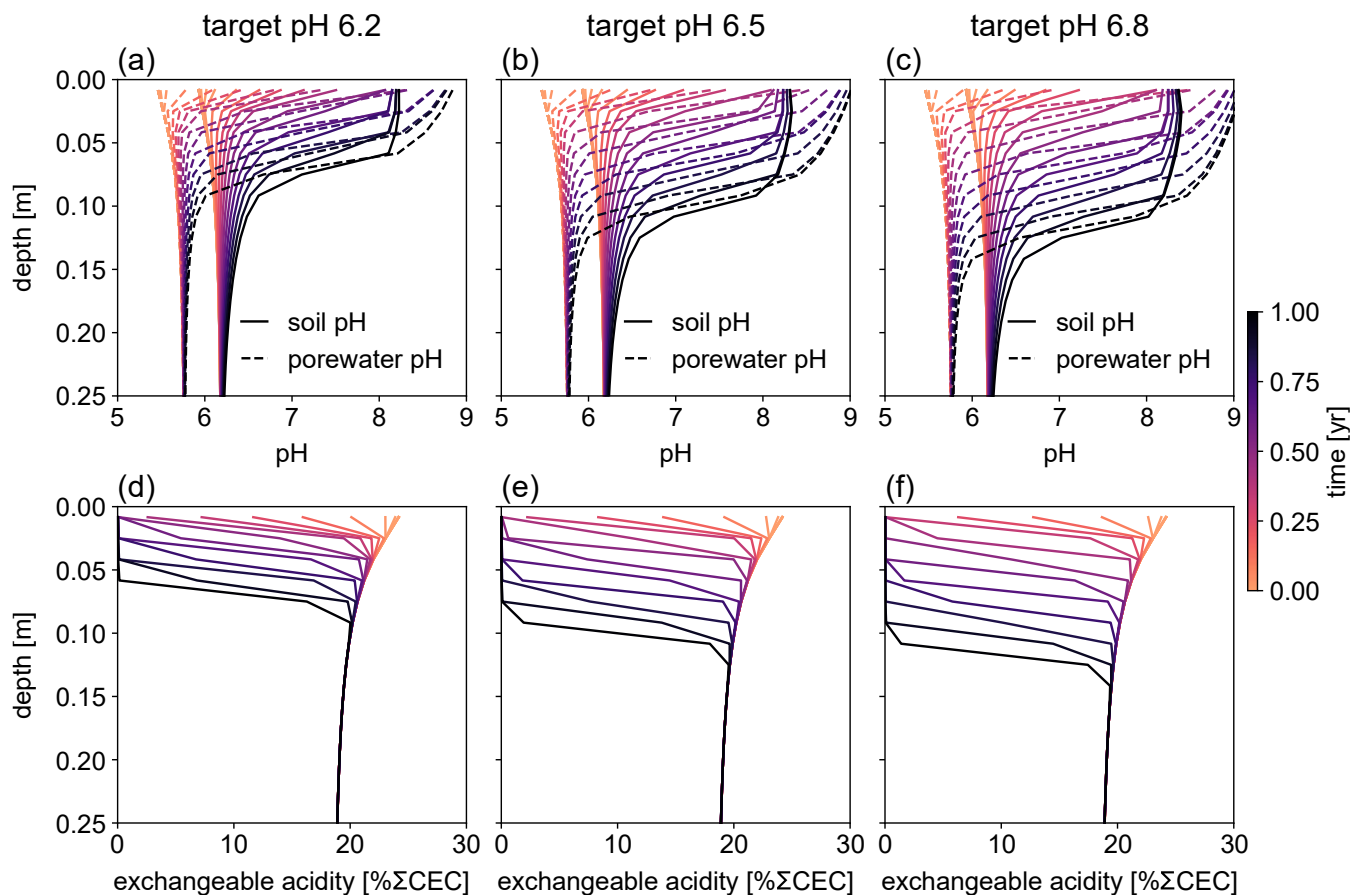
**Figure 7:** Evolution of soil and porewater pH (a-c) and exchangeable acidity (d-f) during the first year following basalt feedstock application at target pH values of 6.2 (a and d), 6.5 (b and e) and 6.8 (c and f) using porewater pH averaged over 0-15 cm as a pH reference.